Sub-aperture piston phase diversity for segmented and multi-aperture systems

Matthew R. Bolcar* and James R. Fienup

The Institute of Optics, The University of Rochester, Rochester, New York 14627, USA

*Corresponding author: mrbolcar@gmail.com

Received 2 June 2008; accepted 7 July 2008;
posted 27 August 2008 (Doc. ID 96884); published 24 September 2008

Phase diversity is a method of image-based wavefront sensing that simultaneously estimates the unknown phase aberrations of an imaging system along with an image of the object. To perform this estimation a series of images differing by a known aberration, typically defocus, are used. In this paper we present a new method of introducing the diversity unique to segmented and multi-aperture systems in which individual segments or sub-apertures are pistoned with respect to one another. We compare this new diversity with the conventional focus diversity. © 2008 Optical Society of America

OCIS codes: 100.5070, 100.3020, 110.6770, 120.0120.

1. Introduction

Modern ground-based and space-based observatories are nearing the limits on the size and weight of monolithic primary mirrors, hindering an increase in both light collecting efficiency and imaging resolution. In response, technology is heading in the direction of segmented and multi-aperture systems as the next generation of telescopes. Segmented systems such as the Keck Observatory in Hawaii, the Thirty Meter Telescope (TMT), and the James Webb Space Telescope (JWST) to be launched after 2013 use an array of actuated hexagonal segments to create a primary mirror that is easier to fabricate than a monolithic mirror of equivalent size, and, in the case of the JWST, capable of being stowed in a launch vehicle and deployed in orbit. Proposed multi-aperture systems, such as the Terrestrial Planet Finder Interferometer [1], Keck Interferometer, and MIDAS [2] use an array of afocal telescopes that are interferometrically combined to achieve a resolution comparable to a primary mirror equivalent to the entire array size.

In either configuration, the segments or sub-apertures must be aligned to very tight tolerances in order to achieve the resolution benefit of the entire array. Some form of actuation is necessary to maintain equivalent optical path distances (OPDs) between the segments or sub-apertures. In the case of segmented systems such as the JWST, actuation is achieved by mounting each hexagonal segment on a hexapod, allowing for seven degrees of freedom: x and y translation, clocking, piston, tip, tilt, and intra-segment radius of curvature. For multi-aperture systems, a system of optical delay lines equalizes the path length between each sub-aperture. These optical delay lines are tunable, allowing for adjustments of sub-aperture piston phase, and in some cases tip and tilt.

It is necessary to know the state of each segment or sub-aperture to within a small fraction of a wavelength in order to apply the appropriate corrections to the actuators. Given the complexity of modern segmented and multi-aperture systems, laser interferometry is not a practical method of wavefront sensing; furthermore, frequent recalibration is likely necessary due to drift in the mechanical mounting and actuating systems. Shack–Hartmann wavefront sensors have proved useful for large ground-based systems, but generally do not work as well for extended objects or for wavefronts having high complexity. Laser guide stars can provide an isolated point source for ground-based systems, but do not work

0003-6935/09/0100A5-08$15.00/0

for space-based systems since they use the properties of the sodium layer of the upper atmosphere.

Image-based wavefront sensing techniques such as phase retrieval and phase diversity allow for an estimate of the pupil phase to be made directly from images produced by the system and have been identified as enabling technologies for space-based systems, where the aberrations do not change with extreme rapidity. Phase retrieval algorithms require a known object which is usually an unresolved point source. Phase diversity algorithms do not require the object to be known and will estimate the object in addition to the system phase.

Phase diversity was first proposed as a method of wavefront sensing by Gonsalves [3] and later developed by Paxman and Fienup for multi-aperture systems [4]. Paxman, Schulz, and Fienup formulated phase diversity from a statistical model that better captured the affect of noise on the algorithms [5]. Further developments by Paxman and Seldin combined the method of phase diversity with speckle imaging and introduced a broadband model of phase diversity incorporating a gray-world model of the object [6] that was later tested by Bolcar and Fienup [7]. In this paper we continue the development of phase diversity by utilizing the unique architecture of segmented and multi-aperture systems to introduce sub-aperture piston phase as the diversity function, as an alternative to focus diversity. This technique of sub-aperture piston phase diversity (SAPPD) was first reported in [8]. We include here the effects of a broadband object and algorithm, as well as compare the performance of sub-aperture piston diversity and focus diversity with respect to object reconstruction error.

SAPPD can be useful for Fourier transform imaging spectroscopy with a multi-aperture system [9] where the sub-apertures are purposely pistoned to collect spectral data. Also, SAPPD can be useful as a risk reduction method on systems where the focus diversity mechanism fails or is disabled.

In Section 2 we review the phase diversity concept, incorporating the statistical techniques of [5] and the broadband techniques of [6,7] and introducing the implementation of sub-aperture piston phase. In Section 3 we describe digital simulations that compare SAPPD to conventional focus diversity. In Section 4 we present the results and in Section 5 we summarize and conclude the paper.

2. Statement of Problem

A. Image Model

The detected images are modeled as

$$d_k(u,v) = \sum_{\lambda} f_{\lambda}(u,v) * s_{k,\lambda}(u,v) + n_k(u,v), \qquad (1)$$

where d_k is the kth detected image, (u,v) are the image plane coordinates, f_λ are the object pixel values at wavelength λ, $s_{k,\lambda}$ is the kth intensity point spread function (PSF) at wavelength λ, n_k is the noise in the kth image, and * denotes a convolution. The intensity PSF is the magnitude squared of the coherent impulse response,

$$s_{k,\lambda}(u,v) = |h_{k,\lambda}(u,v)|^2, \qquad (2)$$

which in turn is a Fresnel-like transform of the pupil,

$$\begin{aligned} h_{k,\lambda}(u,v) = &\exp\left[i\frac{\pi D_k}{\lambda B_k}(u^2+v^2)\right] \\ &\times \int\int P_{k,\lambda}(x,y)\exp\left[i\frac{\pi A_k}{\lambda B_k}(x^2+y^2)\right] \\ &\times \exp\left[-i\frac{2\pi}{\lambda B_k}(xu+yv)\right]dxdy, \end{aligned} \qquad (3)$$

where (x,y) are the pupil plane coordinates and A_k, B_k, and D_k are the elements of the ABCD ray-transfer matrix that relates the pupil plane to the image plane [10] for the kth diversity image. The generalized pupil, $P_{k,\lambda}(x,y)$, is given by a sum over the sub-aperture functions,

$$\begin{aligned} P_{k,\lambda}(x,y) &= \sum_{q=1}^{Q} P_{q,k,\lambda}(x,y) \\ &= \sum_{q=1}^{Q} |P_q(x,y)| \\ &\quad \times \exp\left\{i\frac{2\pi}{\lambda}[W_q(x,y) + W_{q,k}^{\mathrm{div}}(x,y)]\right\}, \end{aligned} \qquad (4)$$

where Q is the number of sub-apertures or segments, W_q is the unknown contribution of the phase on sub-aperture q in terms of optical path delay (OPD), and $W_{q,k}^{\mathrm{div}}$ is the known diversity contribution to the phase on sub-aperture q in terms of OPD.

The unknown OPD, $W_q(x,y)$, can be parameterized in a number of ways. The most straightforward method is as a pixel-by-pixel phase map,

$$W_q(x,y) = \sum_{m,n} \alpha_{q,m,n}\delta(x - m\Delta x, y - n\Delta y), \qquad (5)$$

where $\alpha_{q,m,n}$ is the value of the OPD at pixel index (m,n) in the qth sub-aperture, $(\Delta x, \Delta y)$ are the pixel spacings, and δ is a delta function. Another popular method is to estimate the phase by an expansion over basis functions:

$$W_q(x,y) = \sum_{j=1}^{J} \alpha_{q,j} Z_{q,j}(x,y), \qquad (6)$$

where J is the number of terms in the expansion and $Z_{q,j}(x,y)$ is the jth basis function defined over the qth sub-aperture. Zernike-like polynomials are commonly chosen for the expansion since each

polynomial represents a balanced optical aberration. In either representation, the phase is parameterized in terms of the vector of coefficients, $\boldsymbol{\alpha}$.

The goal of phase diversity is to estimate the phase parameters, $\boldsymbol{\alpha}$, and the object pixels, $f_\lambda(u,v)$, at each wavelength λ, from the set of detected images $\{d_k(u,v)\}$.

B. Nonlinear Optimization

In [5], the phase diversity problem is formulated as a nonlinear optimization in which the appropriate likelihood function is maximized for a given noise mechanism. We follow the same treatment here and maximize the Gaussian log-likelihood function in the Fourier domain, given by

$$\mathbf{L}[\{d_k(u,v)\};\mathbf{f},\boldsymbol{\alpha}] = -\sum_{k=1}^{K}\sum_{f_u f_v}\left|D_k(f_u,f_v) - \sum_{\lambda}F_\lambda(f_u,f_v)S_{k,\lambda}(f_u,f_v)\right|^2, \quad (7)$$

where now $\mathbf{f} = \{f_\lambda(u,v)\}$ is an estimate of the object, K is the number of diversity images, (f_u,f_v) are spatial frequency coordinates, D_k is the Fourier transform of the kth detected image, F_λ is the Fourier transform of the object estimate at wavelength λ, and $S_{k,\lambda}$ is the kth optical transfer function (OTF) estimate at wavelength λ.

Maximizing Eq. (7), or equivalently minimizing the negative of Eq. (7), with respect to $\mathbf{f}$ and $\boldsymbol{\alpha}$ provides an estimate of the object pixel values and phase parameters. If the phase is parameterized as polynomial coefficients and is limited to J terms, and an $M \times N$ array of pixels at L spectral bands of the object is estimated, the dimensionality of the search space of the optimization is given by $M \times N \times L + J$. For example, a moderately sized problem including 45 polynomial coefficients, 5 spectral bands, and a 256×256 pixel region of the object requires searching a 327,000-dimensional space, the bulk of which is due to the estimation of the object.

Gonsalves derived a method [3] that involves substituting an estimate of the object into Eq. (7) that reduces the metric to a function of only the phase parameters. The most common execution of Gonsalves' method uses an inverse-filtered version of the object as an object estimate for a given phase estimate. To make this work for broadband objects, a gray-world assumption must first be made, where it is assumed that each pixel in the object has the same spectrum,

$$f_\lambda(u,v) = \Phi_\lambda f(u,v), \quad (8)$$

where Φ_λ is a spectral coefficient at wavelength λ. Under this assumption, the reduced Gaussian metric becomes

$$\mathbf{L}_{\mathrm{RG}}[\{d_k(u,v)\};\boldsymbol{\alpha}] = \sum_{f_u f_v \in \chi}\left\{\sum_{k=1}^{K}|D_k|^2 - \frac{\left|\sum_{j=1}^{K}D_j\sum_{\lambda}\Phi_\lambda S^*_{j,\lambda}(\boldsymbol{\alpha})\right|^2}{\sum_{m=1}^{K}\left|\sum_{\lambda}\Phi_\lambda S_{m,\lambda}(\boldsymbol{\alpha})\right|^2}\right\}, \quad (9)$$

where χ is the set of pixels where the denominator does not equal zero and the dependence of D_j and $S_{j,\lambda}$ on (f_u,f_v) has been left out for brevity. Notice the object does not appear explicitly in Eq. (9). Instead, the object is implicitly estimated jointly with the phase parameters when the metric is minimized. After the phase is estimated, the object can be reconstructed with a Wiener–Helstrom filter.

Numerous regularization schemes have been proposed for improving the robustness of the reduced Gaussian metric with respect to noise [11–14]. For this work we use only the regularization imposed by restricting the summation over χ. Furthermore, we assume the spectral coefficients Φ_λ are known *a priori*.

Typically, Eq. (9) is minimized with a gradient search algorithm. To assist the computation and avoid costly finite difference calculations, analytic gradients of the metric with respect to the unknown phase parameters can be computed and are given by

$$\frac{\partial \mathbf{L}_{RG}}{\partial \alpha_{\xi,j}} = 8\pi\mathrm{Im}\left\{\sum_{k=1}^{K}\sum_{\lambda}\frac{\Phi_\lambda}{\lambda}\sum_{f'_u f'_v}Z_{\xi,j}(f'_u,f'_v)P_{\xi,k,\lambda}(f'_u,f'_v) \times \exp\left[i\frac{\pi A_k}{\lambda B_k}(f'^2_u + f'^2_v)\right] \times \sum_{f_u f_v \in \chi}Y^*_k(f_u,f_v)H^*_{k,\lambda}(f'_u - f_u, f'_v - f_v)\right\}, \quad (10)$$

where $H_{k,\lambda}$ are the generalized pupil functions given by

$$H_{k,\lambda}(f_u,f_v) = P_{k,\lambda}(f_u,f_v)\exp\left[i\frac{\pi A_k}{\lambda B_k}(f_u^2 + f_v^2)\right], \quad (11)$$

and

$$Y_k(f_u,f_v) = \frac{\sum_{m=1}^{K}\left|\sum_{\lambda}\Phi_\lambda S_{m,\lambda}\right|^2\left(\sum_{\ell=1}^{K}D_\ell\sum_{\lambda}\Phi_\lambda S^*_{\ell,\lambda}\right)D^*_k - \left|\sum_{\ell=1}^{K}D_\ell\sum_{\lambda}\Phi_\lambda S^*_{\ell,\lambda}\right|^2\sum_{\lambda}\Phi_\lambda S^*_{k,\lambda}}{\left(\sum_{m=1}^{K}\left|\sum_{\lambda}\Phi_\lambda S_{m,\lambda}\right|^2\right)^2}. \quad (12)$$

Equations (10) and (12) are similar in form to Eqs. (25) and (26) in [15].

3. Digital Simulations

A triarm-9 aperture was modeled in digital simulation to compare the two types of phase diversity, quadratic and sub-aperture piston, through a series of Monte Carlo simulations. The amount of each type of diversity was varied, and for each amount of diversity three images were simulated, one image with no diversity phase and two images with equal but opposite amounts of diversity phase. Figure 1 shows the sub-aperture piston phase and focus diversity implementations used. Each type and magnitude of diversity was then tested at varying levels of signal-to-noise ratio (SNR).

For these simulations, a hyperspectral AVIRIS [16] data cube was used as the object. We extracted a spectral bandwidth of 96 nm centered about 1 μm with 10 nm separation between adjacent wavelengths ($L = 11$ bands). Since the object was not truly gray-world, the spectrum averaged over all of the pixels was used for the spectral coefficients, Φ_λ. Figure 2 shows a panchromatic representation of the 350×350 object. Note that in the simulations the images were computed without the gray-world assumption, as in Eq. (1), but in our reconstructions we used the gray-world assumption, a realistic model mismatch.

Five independent phase realizations were tested with an average RMS wavefront error of 0.18λ, which consisted of global Zernike terms up to 6th order and sub-aperture Zernike terms up to 2nd order. A representative phase realization is shown in Fig. 3. For each phase realization, five independent noise realizations were simulated. The results were then averaged over the 25 trials.

Three criteria are used here to compare the two types of diversity. The first criterion is the error in the phase estimation, which must be insensitive to global piston, tip, and tilt phase errors, which the phase diversity algorithm cannot estimate and do not affect image quality. We choose to quantify the phase error in terms of the Strehl ratio, given by

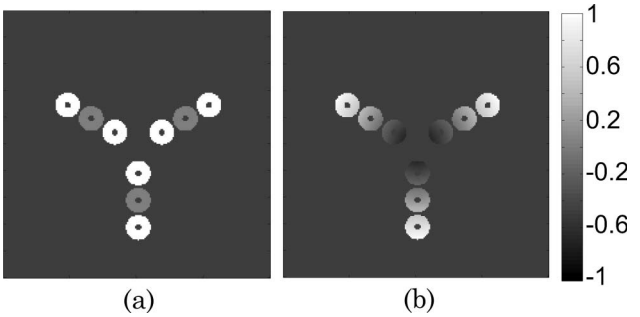

Fig. 1. Example of phase diversity implementation: (a) sub-aperture piston diversity, (b) focus diversity. The scale has units of waves.

Fig. 2. Panchromatic representation of multi-spectral object. The object consists of 11 spectral bands, centered about 1 μm and spanning 96 nm.

$$S.R. = \frac{\max_{u,v}[s_{\text{res}}(u,v)]}{s_{\text{per}}(0,0)}, \tag{13}$$

where s_{per} is the PSF resulting from an aberration-free pupil and s_{res} is the PSF resulting from a pupil aberrated by the residual OPD error, $W_{\text{res}}(x,y) = W_{\text{act}}(x,y) - W_{\text{est}}(x,y)$, where W_{act} is the actual OPD of the pupil and W_{est} is the OPD estimated by the algorithm. A Strehl ratio near unity corresponds to accurate phase estimation. To accurately evaluate the maximum in Eq. (13), the PSFs are upsampled by a factor of 10 using a fast, efficient upsampling algorithm by matrix-multiply discrete Fourier transform (DFT) [17,18].

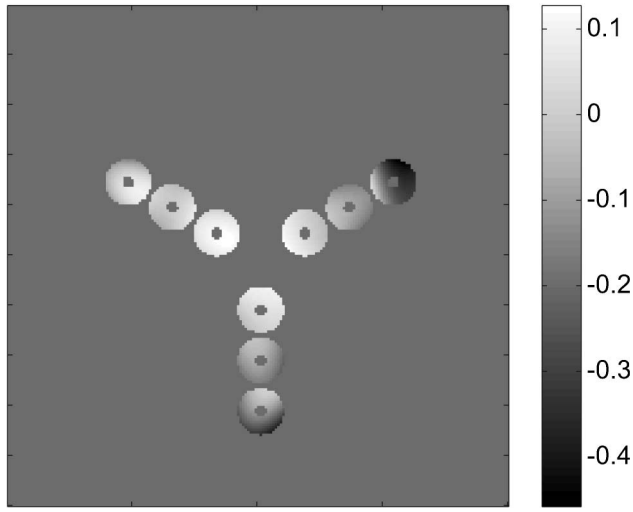

Fig. 3. Example phase realization composed of up to 6th order Zernike terms on the global aperture and up to 2nd order Zernike terms on each sub-aperture. The scale has units of waves.

The second criterion of comparison is the amount of computation required by each type of diversity, quantified by the number of iterations required before the algorithm met the exit criteria. The amount of time involved in evaluating the error metric and its gradients was nearly identical for each type of diversity. Therefore, comparing the number of iterations provides a comparison of the computational burden of each type of diversity.

The final criterion is the error in the reconstructed object. A multi-frame Wiener–Helstrom filter is computed using the estimated phase [19] and then used to reconstruct a gray-world image of the object. For a fair comparison, a series of diffraction-limited, gray-world images were simulated and noise was added,

$$d_{\mathrm{DL}}(u,v) = \left[\sum_{\lambda} f_{\lambda}(u,v)\right] * \left[\sum_{\lambda} s_{\mathrm{DL},\lambda}(u,v)\right] + n(u,v), \tag{14}$$

with similar noise statistics as the aberrated images. The multi-frame Wiener–Helstrom filter provides an SNR benefit according to the number of frames being used. Since the diffraction-limited images have no phase diversity, just three frames were simulated, each with a different noise realization, for each SNR level. This allows for a comparable SNR benefit from the multi-frame Wiener–Helstrom filter as the aberrated diverse images would achieve.

The reconstructed, aberrated, gray-world images were then compared to the reconstructed, diffraction-limited, gray-world images by means of a normalized root mean squared error (NRMSE) metric that is invariant with image translation [18].

4. Results

A. Phase Estimation

Figure 4 shows the results for the Strehl ratio for three SNRs. Focus diversity exhibits expected behavior giving the best performance for one to two waves of focus diversity. Piston diversity shows a different behavior. As the amount of diversity increases, the phase estimation goes through a cycle. At integer values of the center wavelength of the band, the piston diversity performs very poorly, because at integer wavelength values there is little diversity, unless the spectral bandwidth is very large. In these simulations, the bandwidth was a modest 10%. However, piston diversity performs well for non-integer numbers of wavelengths. At half-integer values of the center wavelength a slight decrease in performance is seen due to the fact that for small bandwidths there are effectively only two diversity images, one in-focus and one with only a half wave of diversity. For these examples, at the optimum diversity value for each type of diversity, focus diversity performed better than SAPPD for low SNR, but SAPPD performed better at high SNRs.

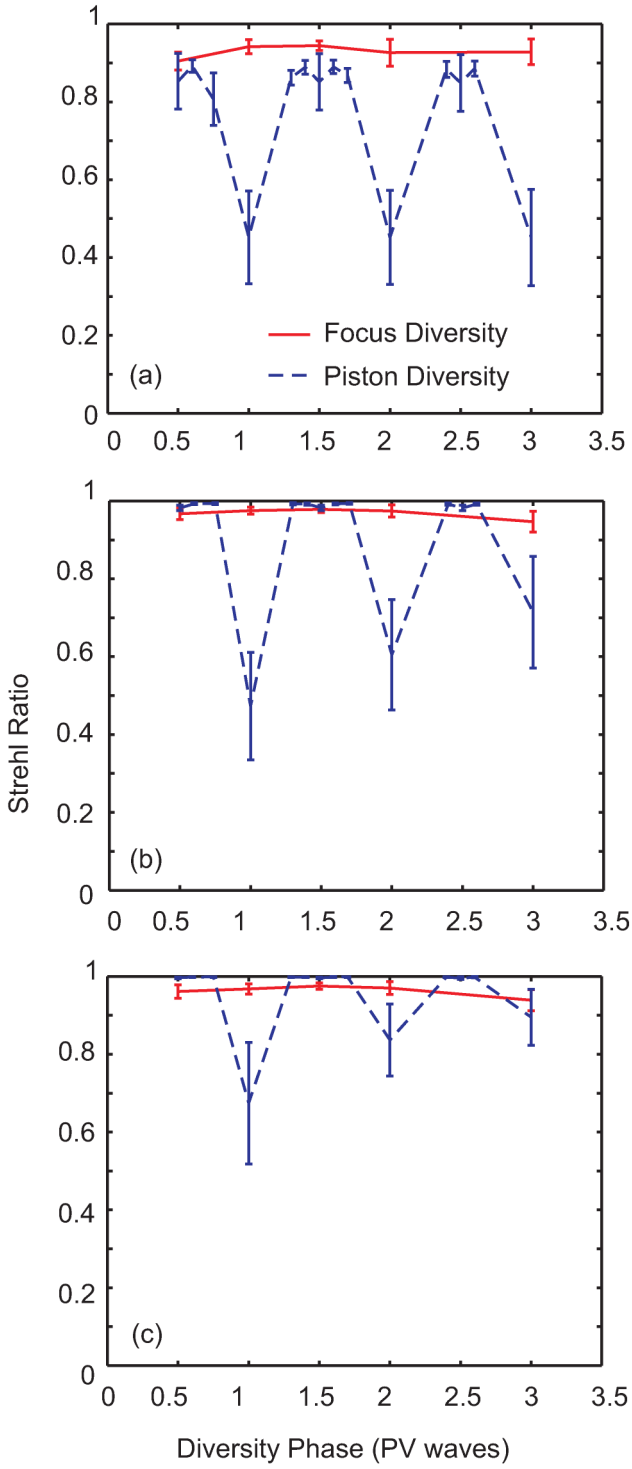

Fig. 4. (Color online) Phase estimation results in terms of Strehl ratio: (a) average pixel SNR of 20, (b) SNR 74, (c) SNR 170. Vertical axis shows Strehl ratio, horizontal axis is the peak-to-valley amount of diversity in units of waves. Each data point is an average of 25 trials (5 phase realizations × 5 noise realizations); error bars show a single standard deviation.

B. Computational Burden

Figure 5 shows the number of iterations required before the algorithm reached its exit criteria. The algorithm typically stops iterating when there is no

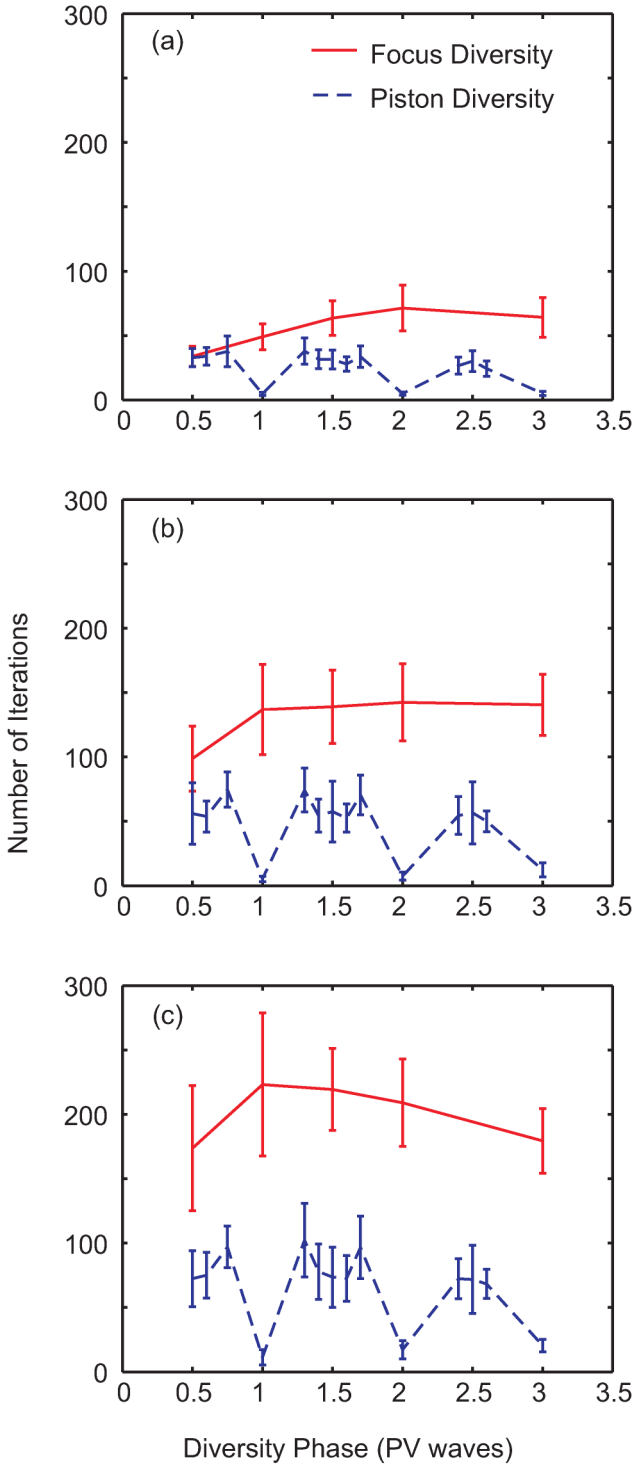

Fig. 5. (Color online) Number of iterations before algorithm reaches exit criteria: (a) average pixel SNR of 20, (b) SNR 74, (c) SNR 170. Vertical axis shows the number of iterations, horizontal axis is the peak-to-valley amount of diversity in units of waves. Each data point is an average of 25 trials; error bars show a single standard deviation.

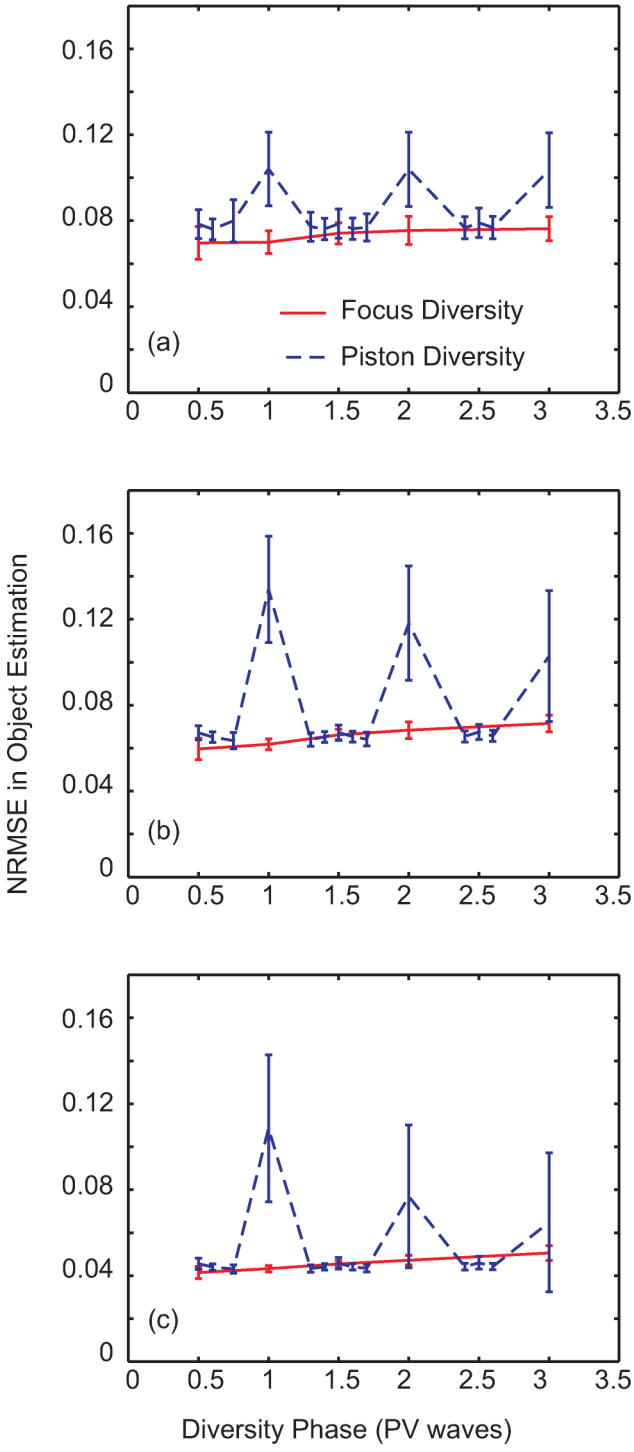

Fig. 6. (Color online) Normalized RMS error between reconstructed aberrated object and reconstructed diffraction-limited object: (a) average pixel SNR of 20, (b) SNR 74, (c) SNR 170. Vertical axis shows NRMSE, horizontal axis is the peak-to-valley amount of diversity in waves. Each data point is an average of 25 trials; error bars show a single standard deviation.

significant change in either the error metric value or parameters being estimated. This corresponds to finding a minimum value of the objective function, which may or may not be the global minimum. For both types of diversity, the algorithm took fewer iterations when phase estimation was poor. This may indicate that the algorithm was getting trapped in a local minimum and that restarting the algorithm with a different initial guess might be beneficial.

Overall, sub-aperture piston phase diversity took fewer iterations than conventional focus diversity.

C. Object Estimation

Figure 6 shows the normalized root mean squared error in the reconstructed objects. For phase diversity at an integer number of waves of the center wavelength, where the phase estimate is poor, SAPPD gives a poor object reconstruction. However, SAPPD gives a good object reconstruction nearer to half-integer waves of diversity, and the error does not appear to increase with the amount of diversity since the suppression of the OTF does not significantly change with the magnitude of the piston diversity. In comparison, the OTF becomes increasingly suppressed as quadratic phase diversity is increased. Overall, when both types of diversity yield a good reconstruction, the NRMSE is comparable.

Figure 7 shows an example reconstruction for an SNR of 74 using SAPPD. Figure 7(a) shows the gray-world image reconstructed using the phase estimated from the phase diversity algorithm using sub-aperture piston diversity values of $[-1.5, 0, 1.5]\lambda$, in good agreement with the diffraction-limited, gray-world, reconstructed image shown in Fig. 7(b). For comparison, Fig. 7(c) shows the zero-diversity aberrated imagery that was used as input to the phase diversity algorithm; the reconstructed images are greatly improved over the best measured image.

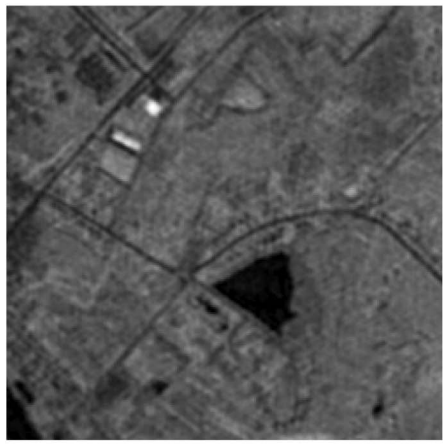

(a)

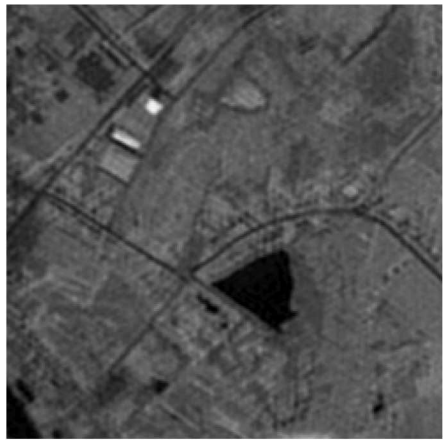

(b)

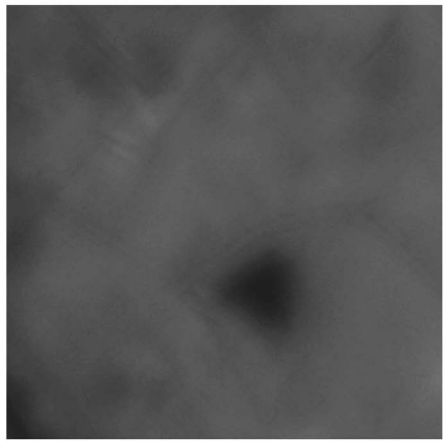

(c)

Fig. 7. Example reconstructed images: (a) reconstructed gray-world image using phase estimate from phase diversity algorithm, (b) reconstructed gray-world diffraction-limited image, (c) original aberrated, zero-diversity image used as input to phase diversity algorithm. All images are shown on same color scale; SNR 74.

5. Summary

We introduced a new method of implementing phase diversity on segmented and multi-aperture systems that utilizes control of the individual segments or sub-apertures. Instead of adding defocus phase to each diversity image, a subset of the segments or sub-apertures was pistoned with respect to the others to introduce the diversity. A series of Monte Carlo simulations was run to compare sub-aperture piston phase diversity to conventional focus phase diversity. In each case, performance was compared for varying amounts of diversity and varying levels of SNR.

It was shown that focus diversity generally estimates the phase better than SAPPD for low SNR, with the reverse being true for high SNR. Piston phase diversity performed well when non-integer values of the center wavelength are chosen for the amount of diversity. In practice one could select this favorable amount of diversity. SAPPD uniformly required substantially less computation before reaching a minimum value of the error metric than focus diversity. Finally, both focus diversity and SAPPD provide comparably good object reconstructions when the phase estimation is also good.

SAPPD proves to be a useful type of phase diversity for segmented and multi-aperture systems where pistoning of sub-apertures is allowable. Future work will explore the use of segment tip and tilt as the diversity function, as most segmented systems include these degrees of freedom. SAPPD may be especially useful as a risk reduction technique for systems if the primary focus diversity mechanism fails.

This work was funded by a Graduate Student Research Fellowship sponsored by NASA Goddard Space Flight Center.

References

1. TPF Science Working Group, *Terrestrial Planet Finder Interferometer: Science Working Group Report*, P. R. Lawson, O. P. Lay, K. J. Johnston, and C. A. Beichman, eds., JPL Publication 07-01 (Jet Propulsion Laboratory, 2007).
2. J. T. Pitman, A. Duncan, D. Stubbs, R. D. Sigler, R. L. Kendrick, E. H. Smith, J. E. Mason, G. Delory, J. H. Lipps, M. Manga, J. R. Graham, I. de Pater, S. Reiboldt, P. Marcus, E. Bierhaus, J. B. Dalton, J. R. Fienup, and J. W. Yu, "Multiple Instrument Distributed Aperture Sensor (MIDAS) for planetary remote sensing," Proc. SPIE **5660**, 168–180 (2004).
3. R. A. Gonsalves and R. Chidlaw, "Wavefront sensing by phase retrieval," Proc. SPIE **207**, 32–39 (1979).
4. R. G. Paxman and J. R. Fienup, "Optical misalignment sensing and image reconstruction using phase diversity," J. Opt. Soc. Am. A **5**, 914–923 (1988).
5. R. G. Paxman, T. J. Schulz, and J. R. Fienup, "Joint estimation of object and aberrations by using phase diversity," J. Opt. Soc. Am. A **9**, 1072–1085 (1992).
6. R. G. Paxman and J. H. Seldin, "Fine-resolution astronomical imaging with phase-diverse speckle," Proc. SPIE **2029**, 287–298 (1993).
7. M. R. Bolcar and J. R. Fienup, "Phase diversity with broadband illumination," in *Adaptive Optics: Analysis and Methods/Computational Optical Sensing and Imaging/Information Photonics/Signal Recovery and Synthesis Topical Meetings on CD-ROM*, OSA Technical Digest (CD) (Optical Society of America, 2007), paper JTuA6.
8. M. R. Bolcar and J. R. Fienup, "Method of phase diversity in multi-aperture systems utilizing individual sub-aperture control," Proc. SPIE **5896**, 58960G (2005).
9. S. T. Thurman and J. R. Fienup, "Multi-aperture Fourier transform imaging spectroscopy: theory and imaging properties," Opt. Express **13**, 2160–2175 (2005).
10. J. Goodman, *Introduction to Fourier Optics*, 3rd ed. (Roberts & Co., 2004).
11. D. J. Lee, M. C. Roggemann, B. M. Welsh, and E. R. Crosby, "Evaluation of least-squares phase-diversity techniques for space telescope wave-front sensing," Appl. Opt. **36**, 9186–9197 (1997).
12. O. M. Bucci, A. Capozzoli, and G. D'Elia, "Regularizing strategy for image restoration and wave-front sensing by phase diversity," J. Opt. Soc. Am. A **16**, 1759–1768 (1999).
13. M. G. Löfdahl and G. B. Scharmer, "Phase diverse speckle inversion applied to data from the Swedish 1-meter solar telescope," Proc. SPIE **4853**, 567–575 (2002).
14. A. Blanc, L. Mugnier, and J. Idier, "Marginal estimation of aberrations and image restoration by use of phase diversity," J. Opt. Soc. Am. A **20**, 1035–1045 (2003).
15. J. H. Seldin, R. G. Paxman, V. G. Zarifis, L. Benson, and R. E. Stone, "Closed-loop wavefront sensing for a sparse-aperture, multiple telescope array using broad-band phase diversity," Proc. SPIE **4091**, 48–63 (2000).
16. Provided through the courtesy of Jet Propulsion Laboratory, California Institute of Technology, Pasadena, California (http://aviris.jpl.nasa.gov/).
17. R. Soummer, L. Pueyo, A. Sivaramakrishnan, and R. J. Vanderbei, "Fast computation of Lyot-style coronagraph propagation," Opt. Express **15**, 15935–15951 (2007).
18. M. Guizar-Sicairos, S. T. Thurman, and J. R. Fienup, "Efficient subpixel image registration algorithms," Opt. Lett. **33**, 156–158 (2008).
19. L. P. Yaroslavsky and H. J. Caulfield, "Deconvolution of multiple images of the same object," Appl. Opt. **33**, 2157–2162 (1994).